ACS OMEGA

Open Access

http://pubs.acs.org/journal/acsodf

Article

Optimizing Electrochemical Deposition for Biodegradable Zinc-Hydroxyapatite Systems in Bone Repair

Radka Gorejova,* Ivana Mojzisova, Evghenii Harea, Tibor Sopcak, and Kadir Ozaltin

Cite This: *ACS Omega* 2026, 11, 1062−1076

Read Online

ACCESS | Metrics & More | Article Recommendations

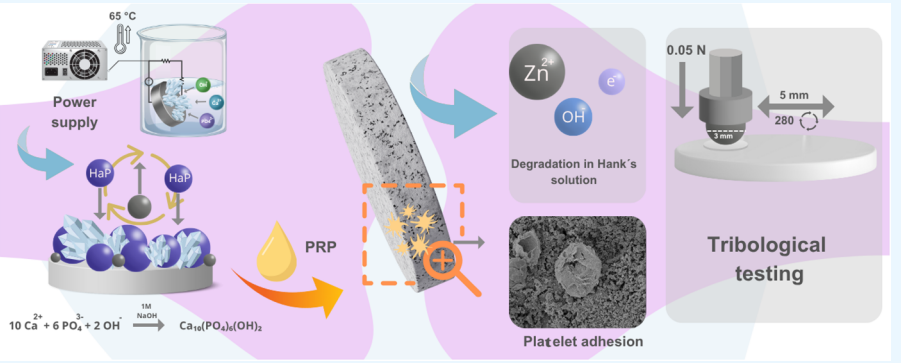

ABSTRACT: Biodegradable metals are gradually gaining increased attention as a new option for complementary treatment alongside standard inert metal implants. While magnesium- and iron-based systems have been extensively studied, zinc has recently emerged as a novel candidate due to its moderate degradation rate and essential biological role. However, the use of pure zinc in biomedical applications is limited by its potential cytotoxicity. A widely adopted strategy to overcome these drawbacks involves surface modification with bioactive ceramic coatings, particularly hydroxyapatite (HAp), to promote bone−material integration. In this study, we report a systematic use of electrochemical deposition (ECD) for the fabrication of hydroxyapatite coatings on zinc substrates. This method allows us to precisely tailor the coating morphology and properties under controlled electrochemical conditions, offering a scalable, low-temperature alternative to other deposition techniques. Key deposition parameters including applied current density, deposition time, and the presence of a chelating agent (EDTA-2Na) were optimized to achieve uniform, adherent, and morphologically favorable HAp layers. The optimal conditions (current density of 1.25 mA/cm^2, deposition time of 120 min, and EDTA-2Na addition) yielded coatings with strong adhesion to the zinc substrate and beneficial HAp morphology for cell-attachment. The ceramic layer not only improved the mechanical stability of the composite system but also reduced the degradation rate in simulated body fluids. Furthermore, the HAp-coated zinc surface did not exhibit any signs of thrombogenicity, suggesting good hemocompatibility.

1. INTRODUCTION

Temporary bone substitutes prepared from biodegradable metals have recently earned increasing attention.[1−7] Among the widely studied metals such as iron[8−12] and magnesium,[13−18] zinc has recently emerged as a material of interest due to its favorable biological properties and degradation in physiological environments.[19−25] In particular, zinc offers a unique balance between biological compatibility and favorable corrosion rates, which makes it a promising candidate for temporary implants, where controlled degradation is required. Zinc, as a biodegradable metal for hard tissue regeneration, is studied in its pure form as well as in alloys[26,27] and composites.[28,29] A primary motivation for developing zinc alloys or composite materials is to mitigate the potential cytotoxicity of Zn implants arising from the excessive release of Zn^{2+} ions during the initial postimplantation phase.[30] The conditional cytotoxicity of biodegradable zinc and its alloys varies based on material composition, test systems, and cell types.[31] Endothelial cells generally show higher viability than L929 fibroblasts, MC3T3-E1 osteoblasts, and vascular smooth muscle cells in cytotoxicity assessments, likely because Zn acts as an antioxidant and membrane stabilizer.[31] It was also reported that uptake up to 15 mol % of zinc in the Zn-HAp nanoparticles did not induce cytotoxicity after 3 days in

Received: August 15, 2025
Revised: September 29, 2025
Accepted: November 5, 2025
Published: December 19, 2025

Table 1. Summary of the Electrochemical Deposition Conditions (Electrolyte Composition, Used Deposition Parameters, After Treatment) for the Preparation of Ceramic Coatings on Zn Substrate

	electrochemical deposition parameters					
	$Ca(NO_3)_2{\cdot}4H_2O$ ($mol{\cdot}dm^{-3}$)	NH_4H_2PO4 ($mol{\cdot}dm^{-3}$)	EDTA-2Na ($mol{\cdot}dm^{-3}$)	after treatment	time of deposition (min)	applied current density ($mA{\cdot}cm^{-2}$)
ZC	$4.2{\cdot}10^{-2}$	$2.5{\cdot}10^{-2}$	-	1 M NaOH for 120 min, 65 °C	30	0.4
ZC-EDTA-1	$4.2{\cdot}10^{-2}$	$2.5{\cdot}10^{-2}$	$7.5{\cdot}10^{-4}$ $mol{\cdot}dm^{-3}$	1 M NaOH for 120 min, 65 °C	30	0.4
ZC-EDTA-2	$4.2{\cdot}10^{-2}$	$2.5{\cdot}10^{-2}$	$7.5{\cdot}10^{-4}$ $mol{\cdot}dm^{-3}$	1 M NaOH for 120 min, 65 °C	120	0.4
ZC-EDTA-3	$4.2{\cdot}10^{-2}$	$2.5{\cdot}10^{-2}$	$7.5{\cdot}10^{-4}$ $mol{\cdot}dm^{-3}$	1 M NaOH for 120 min, 65 °C	120	1.25

preosteoblast cells.[32] Besides that, studies of the anticoagulation properties of blood-containing materials are of huge importance.[33]

Although zinc plays a crucial role in the human body as an essential element involved in bone formation and regeneration processes,[19,22,25,32] its potential toxicity remains a significant barrier to clinical application. Several strategies have been proposed to counteract the potential toxic effects of zinc ions, such as alloying zinc with different elements (Mg, Gd, Y, Ca, etc.)[34−39] or surface modifications.[40] Among these strategies, surface modification represents a particularly attractive approach because it directly influences the degradation behavior at the implant−tissue interface. One common method is the application of protective or bioactive coatings. Previous studies have demonstrated that a ceramic surface, specifically hydroxyapatite (HAp), can reduce the corrosion rate of metallic materials.[41,42] Moreover, hydroxyapatite represents a vital mineral component of natural human bone and plays a significant role in its remodeling. HAp has been shown to positively influence osteoconduction, osteointegration, and osteoinduction (depending on conditions).[29,43−47] Unlike inert coatings, bioactive ceramics such as HAp undergo slight dissolution under physiological conditions, forming a biological apatite layer that enables atomic-level interactions with tissues and the creation of direct chemical bonds with bone.[47] This not only enhances osteogenic responses but also improves mechanical stability under physiological loads.[47]

Both the chemical composition and morphology of the hydroxyapatite layers are critical factors in determining their performance. Variations in elemental substitutions or stoichiometry can alter crystallinity, solubility, and biological activity,[29,38,48] while its morphology is equally important. The morphology of the deposited surface affects cellular adhesion responses expected postimplantation.[49] Hydroxyapatite can exist in various forms depending on the preparation conditions. Several methods such as sol−gel, plasma spraying, sputtering, electrophoresis, pulsed-laser deposition, or microarc oxidation[44,50−53] exist for preparing HAp layers on metallic substrates. Among them, electrochemical deposition (ECD) is a simple, rapid, and cost-effective technique for preparing thin HAp layers on metallic materials, offering extensive variability in preparation conditions (e.g., electrolyte composition, pH, chelating agents, electrochemical parameters) and precursors, enabling tailor-made layers.[41,54−58]

Despite the growing interest in zinc-based biomaterials, only limited work has focused on the direct electrochemical deposition of HAp coatings on zinc substrates. Addressing this gap is crucial for developing effective and clinically relevant Zn-based bone substitutes. Therefore, this study aimed to optimize the electrochemical deposition conditions of HAp layers on Zn metal substrates by varying parameters such as deposition time, current density, and chelating agent usage, thus providing a cost-effective, scalable method for Zn surface modification. The optimized layer exhibiting the best properties was subsequently characterized by using various physicochemical methods. *In vitro* degradation in simulated body fluids, wear behavior, and hemocompatibility were evaluated. To the best of our knowledge, only a few studies have reported the electrochemical deposition of HAp ceramic layers directly on Zn substrates.

2. MATERIALS AND METHODS

2.1. Substrate Preparation. Zinc samples were prepared from a Zn metal powder (99.5% purity, Centralchem, Slovakia). Two grams of Zn powder was cold-pressed using stainless-steel press mold and a hydraulic press (Redats H-380, P.H.U Szczepan, Krakow, Poland) at a pressure of 545 MPa into the cylindrical form with a diameter of 17 mm and a height of ∼4 mm. Prepared green compacts were subsequently sintered using a ceramic furnace (Nabertherm 30−3000, Nabertherm GmbH, Germany) at 350 °C for 1 h in an inert argon (Ar) atmosphere with a gas flow rate of 4 $L{\cdot}min^{-1}$ and let to gradually cool down to laboratory temperature. Prior to ceramic layer deposition, the surface of the specimens was sanded on both sides and around the perimeter with two different sandpaper grits (#600, #1200). The surface grinding was carried out to roughen the surface prior to ceramic layer deposition to achieve better adhesion of the coating. Finally, the samples were ultrasonically cleaned for 10 min in acetone (Centralchem, Slovakia) and in 96% ethanol (Centralchem, Slovakia).

2.2. Ceramic Coating Deposition Optimization. The calcium-phosphate coating was electrochemically deposited from an electrolyte solution containing $4.2{\cdot}10^{-2}$ $mol{\cdot}dm^{-3}$ $Ca(NO_3)_2{\cdot}4H_2O$ and $2.5{\cdot}10^{-2}$ $mol{\cdot}dm^{-3}$ $NH_4H_2PO_4$ using a potentiostat/galvanostat (Autolab Multichannel M204, Metrohm, Switzerland) with a three-electrode system. A cylindrical Zn sample was used as the working electrode, a sheet Pt electrode was used as the auxiliary electrode, and an Ag/AgCl/KCl (3 $mol{\cdot}dm^{-3}$) electrode was used as the reference electrode.

Several electrochemical deposition conditions, summarized in Table 1, were tested during ceramic layer deposition until a suitable quality of the deposited layer was achieved. The varying process parameters were the deposition time, the addition of the chelating EDTA-2Na agent, and the applied current density. The samples were labeled using the abbreviations Z (zinc) and C (ceramic), respectively.

https://doi.org/10.1021/acsomega.5c08241
ACS Omega 2026, 11, 1062−1076

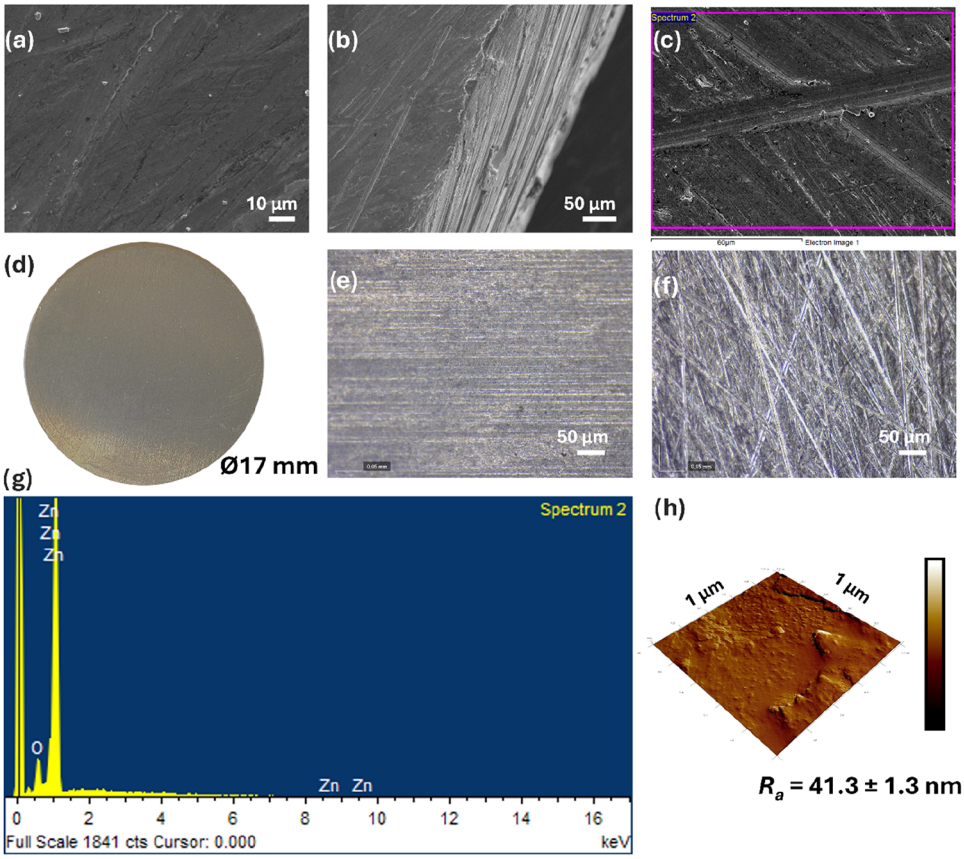

Figure 1. SEM micrographs of Zn substrate (a, c) with detail of the sample edge (b). Optical photograph of the as-sintered Zn sample (d) with detail before (e) and after (f) surface roughening. EDS chemical composition analysis of Zn-sintered sample (g) taken from the area depicted in part (c). AFM examination on Zn surface roughness after sanding (h).

2.3. Surface Characterization. To study the surface of the prepared materials, Dino-Lite AM4815ZT and AM4515T8 digital microscopes (20 to 900× magnification, resolution of 1.3 MPx (Dino-Lite, Delmenhorst, Netherlands)) were used for microscopical observations. To analyze the surface morphology and chemical composition of the prepared layers, a scanning electron microscope (SEM) equipped with an energy-dispersive spectrometer (EDX) was employed (JEOL JSM-7000F, Tokyo, Japan, with EDX INCA analyzer).

Phase composition was examined via X-ray diffraction (XRD) using a Philips X'Pert Pro diffractometer (Cu Kα radiation, 40 kV, 50 mA, with a 2θ range between 10 and 90°, Philips, Netherlands).

Atomic force microscopy (AFM) was employed to examine the surface topology of the sample by using a Dimension Icon microscope (Bruker, Karlsruhe, Germany). The experiments were conducted in peak force tapping mode with a ScanAsyst-Air Si/Nitride probe (Bruker, Santa Barbara, USA), featuring a cantilever spring constant of k = 0.4k = 0.4 N/m. Each sample was scanned over an area of 1 × 1 μm^2 at a frequency of 1 Hz. The average surface roughness (R_a) values were assessed using NanoScope Analysis software.

The Fourier transform infrared (FTIR) spectra were recorded by using an IRTracer-100 infrared spectrometer (Shimadzu, Japan) with the attenuated total reflection (ATR) method.

2.4. Electrochemical Examination of HAp-Coated Samples. The experiments were carried out in a double-wall electrochemical cell, maintained at 37 ± 2 °C and a pH of 7.4 ± 0.2 using an external circulation thermostat, in simulated body fluid (Hanks' solution) with the following composition (g L^{-1}): 8 NaCl, 0.4 KCl, 0.14 $CaCl_2$, 0.06 $MgSO_4 \cdot 7H_2O$, 0.06 $NaH_2PO_4 \cdot 2H_2O$, 0.35 $NaHCO_3$, 1.00 glucose, 0.60 KH_2PO_4, and 0.10 $MgCl_2 \cdot 6H_2O$. Ag/AgCl/KCl (3 mol·dm^{-3}) electrode was used as a reference electrode, platinum (Pt) sheet electrode as a counter electrode, and a cleaned sample as a working electrode. All electrochemical measurements were conducted on Autolab Multichannel M204 potentiostat/galvanostat (Metrohm, Herisau, Switzerland).

To determine the corrosion rate (CR) of the studied samples, potentiodynamic polarization tests (PDP) were carried out along with the open circuit potential (OCP) determination. OCP measurements were taken for 60 min prior to the measurements for the system stabilization. PDP measurements were performed from −250 to +250 mV vs the OCP at a scan rate of 0.1 mV·s^{-1}. The corrosion sample holder (CORR.1LHLD, Metrohm, Herisau, Switzerland) was used to ensure a standard measured area of 1 cm^2. Corrosion rate was determined using the Tafel extrapolation method in NOVA 2.1 software.

2.5. Tribological Testing. Dry sliding friction tests were performed using a Bruker Universal Mechanical Tester (UMT) (Bruker, Santa Barbara, USA) operated in linear ball-on-flat reciprocating mode under ambient conditions (room temperature, air). The ambient relative humidity during testing was maintained at 48 ± 5%. A stainless-steel ball with a 3 mm diameter served as the counter face and was reciprocated against the flat specimen surface.[59] The test was

https://doi.org/10.1021/acsomega.5c08241
ACS Omega 2026, 11, 1062−1076

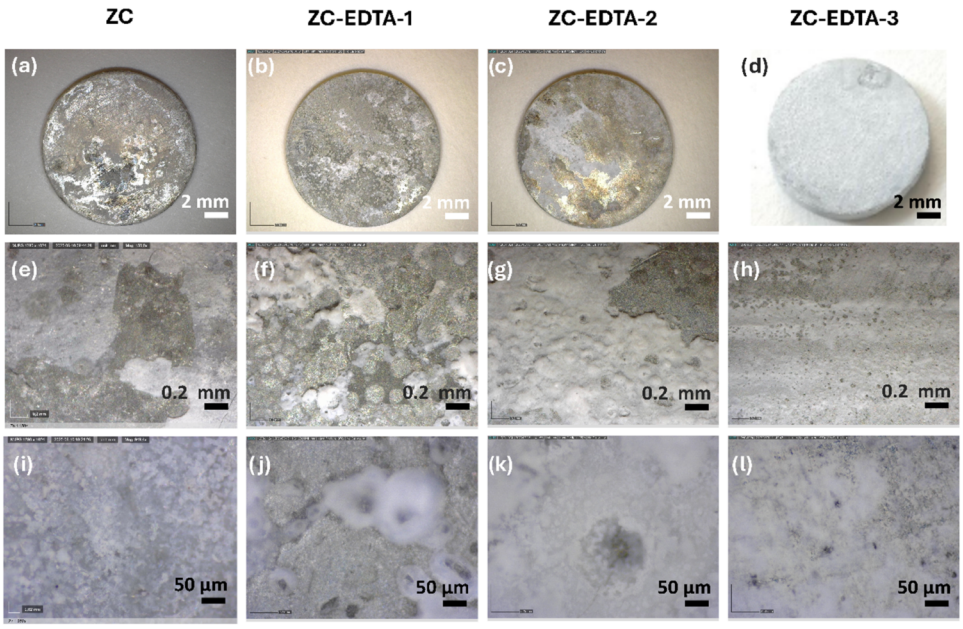

Figure 2. Optical images of zinc-ceramic samples prepared under different electrochemical deposition conditions with different magnifications: macroscopic pictures of the prepared samples (a–d) at 150× magnification (e–h) and 950× magnification (i–l). ZC sample (a, e, i), ZC-EDTA-1 sample (b, f, j), ZC-EDTA-2 sample (c, g, k), and ZC-EDTA-3 sample (d, h, l).

conducted under a constant normal load of 0.05 N, with a stroke length of 5 mm, for a total of 280 cycles over a duration of 280 seconds.

2.6. Hemocompatibility Assessments. To study platelet morphology as an *in vitro* thrombosis parameter, platelet adhesion tests were conducted in triplicate according to the ISO 10993–4 standard for blood interaction assessments. Ethical approval was obtained from the National Ethics Committee ([SK U 01020/599–3/2023–220]). Platelet-rich plasma (PRP) was prepared by centrifuging whole blood at 1600 rpm for 15 min. The resulting samples were disinfected using germicidal UV light for 30 min and then transferred to 24-well plates. Each well received 200 μL of PRP and was incubated at 37 °C for 1 h. Following incubation, samples were rinsed with PBS to remove nonadherent platelets. To fix the adhered platelets on the sample surface, a 2.5% glutaraldehyde solution was applied at room temperature for 12 h. Platelet dehydration was performed using a series of ethanol solutions with increasing concentrations (50, 60, 70, 80, 90, and 100% v/v in water), each applied for 10 min at 4 °C. The samples were then freeze-dried at −12 °C for 4 days. The morphology of the adhered platelets was examined using a scanning electron microscope (SEM) equipped with an energy-dispersive X-ray (EDS) spectrometer (JEOL JSM-7000F, Tokyo, Japan, with EDX INCA analyzer).

3. RESULTS

3.1. Substrate Zn Surface Morphology. Zn samples prepared by the powder metallurgy method were chosen as the substrates for sample preparation. The sintering of the Zn powders produced cylindrical pellets with a height of approximately 4 mm with 17 mm in diameter, which served as a platform for further deposition of the ceramic coating (Figure 1). Any or minimal shrinkage of the sample's volume was observed after sintering (Figure 1d). Immediately after sintering, surface passivation occurred, which led to the formation of a matt layer on the surface of the metallic pellet (Figure 1d). For this reason, the samples were mechanically ground before deposition. This process effectively removed most of the formed oxide layer and created the desired surface roughening for better adhesion of the deposited layer (Figure 1a–f). However, zinc oxide was observed on the surface of the material, even after grinding, which was confirmed by EDS analysis (Figure 1g). Atomic force microscopy was used to evaluate surface roughness before coating, which was demonstrated by the average roughness coefficient (R_a) with a value of 41.3 nm.

3.2. Ceramic Layer Characterization. Ceramic layer deposition was performed as the next step after Zn substrate surface preparation. In the process of HAp coating deposition, four deposition condition sets described in the previous chapter were gradually tested (Figure 2). The process was optimized to the point at which the ceramic layer formed a continuous, homogeneous whitish layer that firmly adhered to the surface of the material. A very uneven coating was prepared with distinct domains, which were not covered by the coating, in the first step (ZC, Figure 2a,e,i). The adhesion of HAp to the Zn surface was low under the given conditions, causing the coating to fall off during deposition and forming areas where HAp was completely absent. In the next step, in addition to changing the electrochemical parameters and the length of the deposition, the chelating agent EDTA-2-Na was added. In the case of the ZC-EDTA-1 (Figure 2b,f,j) and ZC-EDTA-2 (Figure 2c,g,k) sample series, the homogeneous coating was still not reached. The coating was more visible compared to the ZC series; however, recognizable circular uncovered artifacts could be noticed on the surface of the samples (Figure 2f,g). The deposition of final series (ZC-EDTA-3) resulted in samples uniformly coated with a whitish layer of calcium phosphate that was evenly distributed over the entire surface of the coated Zn tablet (except for the electrical contact grip site, Figure 2d). In some places, especially at the edges of the samples, the coating was thinner, and it was possible to observe the substrate shining through. As in the case of the

https://doi.org/10.1021/acsomega.5c08241
ACS Omega 2026, 11, 1062–1076

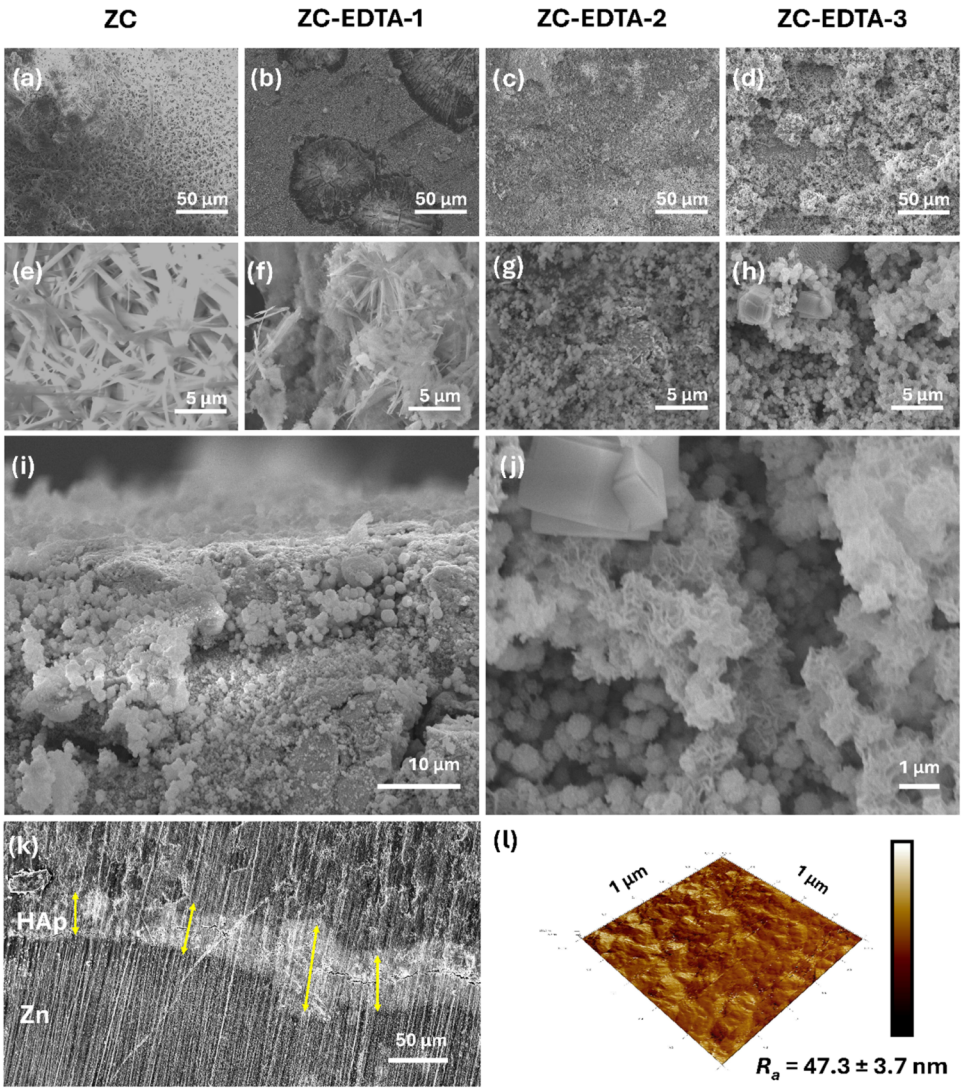

Figure 3. SEM micrographs of zinc-ceramic samples prepared under different electrochemical deposition conditions: (a, e) ZC, (b, f) ZC-EDTA-1, (c, g) ZC-EDTA-2, and (d, h, j) ZC-EDTA-3. Details of the ZC-EDTA-3 sample edge (i) and the details of the surface crystalline structure (j). Cross-section of ZC-EDTA-3 sample with HAp coating (k). AFM image of the ZC-EDTA-3-coated surface (l).

previous series, the ZC-EDTA-3 coating was porous, but the resulting circular defects were significantly smaller (10 ± 2 μm for ZC-EDTA-3 vs 120 ± 30 μm for ZC, ZC-EDTA-1, and ZC-EDTA-2, respectively).

SEM images were taken to study the morphology of the electrochemically deposited coating in more detail (Figure 3). From the images of the coated samples, we can observe that electrochemical deposition of the ceramic coating caused a significant change in the surface morphology of the samples, whereby their surface is formed by numerous crystals that are morphologically distinct from each other. In the case of the ZC (Figure 3a,e) and ZC-EDTA-1 (Figure 3b,f) sample series, it was possible to observe a pronounced needle-like shape of the crystals. While in the case of ZC, we could see uniform, long crystalline formations (Figure 3e), and in the case of ZC-EDTA-1, the needles were irregular, of different lengths, and growing in clusters (Figure 3f). The morphology of the deposited crystals changed in the case of the ZC-EDTA-2 and ZC-EDTA-3 series, when the long needle-like crystals turned into smaller spherical formations. In the case of ZC-EDTA-2 (Figure 3c,g), it was possible to observe many small clusters of spherical crystal formations, which were missing in several places where a layer of Zn substrate was exposed (Figure 3g). In the case of ZC-EDTA-3, the spherical crystals were evenly distributed over the sample surface (Figure 3d,h). In addition to small crystals, large plate-like formations were observed in this series (Figure 3j), which extended from the homogeneous layer. The coated edge of the ZC-EDTA-3 sample is shown in Figure 3i, confirming the coverage of the entire surface of the samples, including the edges. In Figure 3k, the cross-section of the ZC-EDTA-3 sample is illustrated, where the coating layer with an average thickness of 50 ± 14 μm is clearly visible. The average surface roughness after coating slightly increased to R_a = 47.3 nm (Figure 3l).

3.3. Chemical Analysis of Ceramic-Coated Sample Surface. EDS analysis performed during SEM measurements confirmed the presence of calcium, phosphorus, oxygen, and zinc originating from the substrate on the surface of the samples (Figure 4).

The quantitative contribution of individual elements obtained from EDS measurements given in atomic percentages and the expression of the stoichiometric ratio of Ca and P

https://doi.org/10.1021/acsomega.5c08241
ACS Omega 2026, 11, 1062−1076

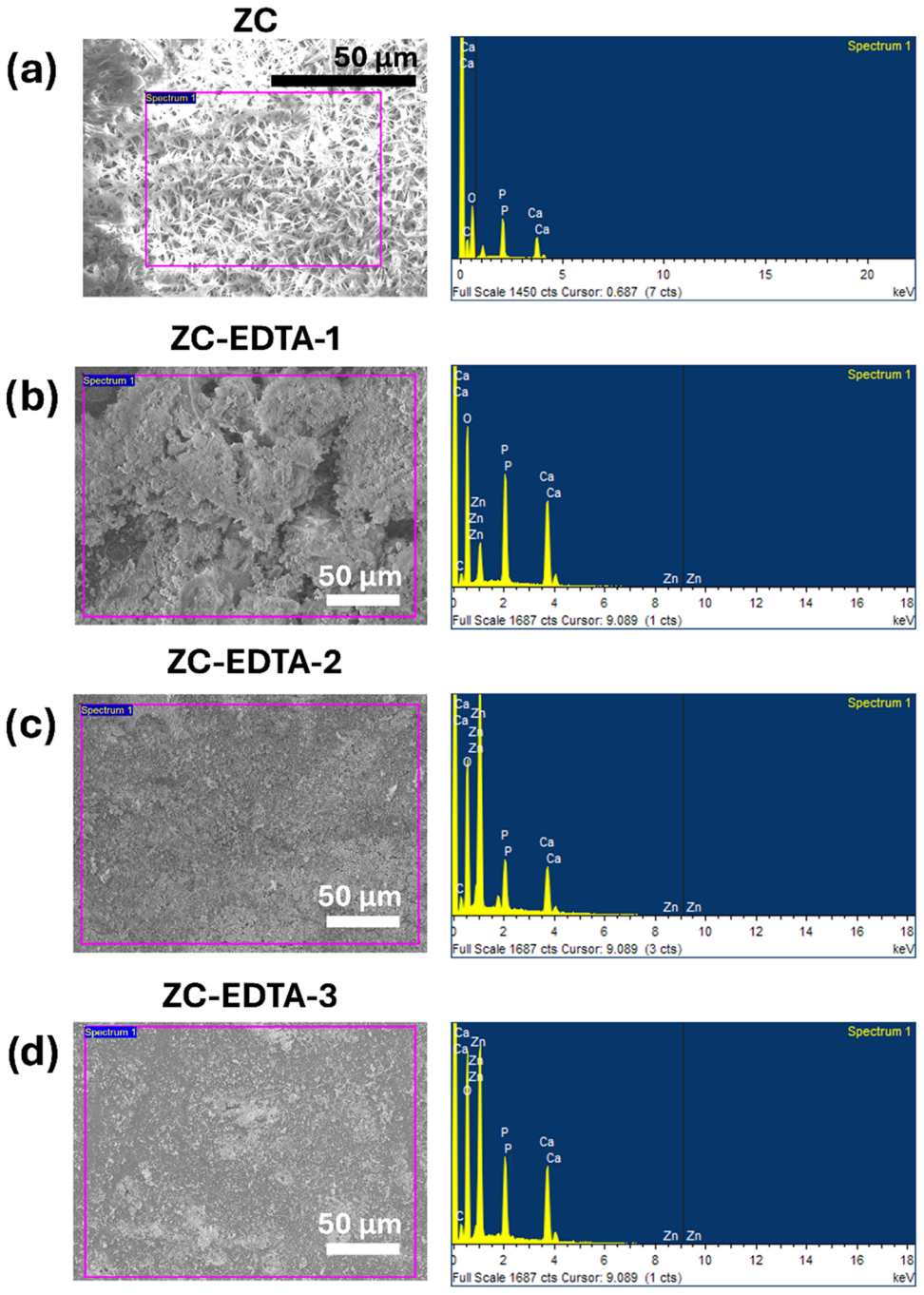

Figure 4. EDS analysis of chemical composition of the prepared ceramic coatings on the zinc substrate: ZC (a), ZC-EDTA-1 (b), ZC-EDTA-2 (c), ZC-EDTA-3 (d).

components for each of the studied sample types are given in Table 2. The Ca/P ratio increased from 0.93 for the ZC sample to 1.47 for the ZC-EDTA-3 sample, which exhibited the highest Ca/P ratio.

FTIR spectroscopy and XRD spectroscopy methods were used to further characterize the deposited layer.

The FTIR spectra of the ceramic-coated samples are shown in Figure 5a. The presence of characteristic functional groups for hydroxyapatite was confirmed for the coated ZC-EDTA-3 sample. The intense, sharp band at 1026 cm^{-1} belongs to the P−O stretching vibration, while the band at 559 cm^{-1} corresponds to the O−P−O bending mode, both originating from the PO_4^{3-} group present in the apatite crystal lattice. A

Table 2. Chemical Composition Analysis of Zinc-Ceramic Samples Prepared under Different Deposition Conditions with Corresponding Ca/P Ratios Obtained from EDS

atom %	ZC	ZC-EDTA-1	ZC-EDTA-2	ZC-EDTA-3
C K	29.56	7.33	11.23	9.35
O K	45.18	54.97	41.89	50.02
P K	13.08	14.67	8.34	10.56
Ca K	12.19	19.57	11.08	15.52
Zn L	-	3.45	27.46	14.55
Ca/P ratio	**0.93**	**1.33**	**1.33**	**1.47**

https://doi.org/10.1021/acsomega.5c08241
ACS Omega 2026, 11, 1062−1076

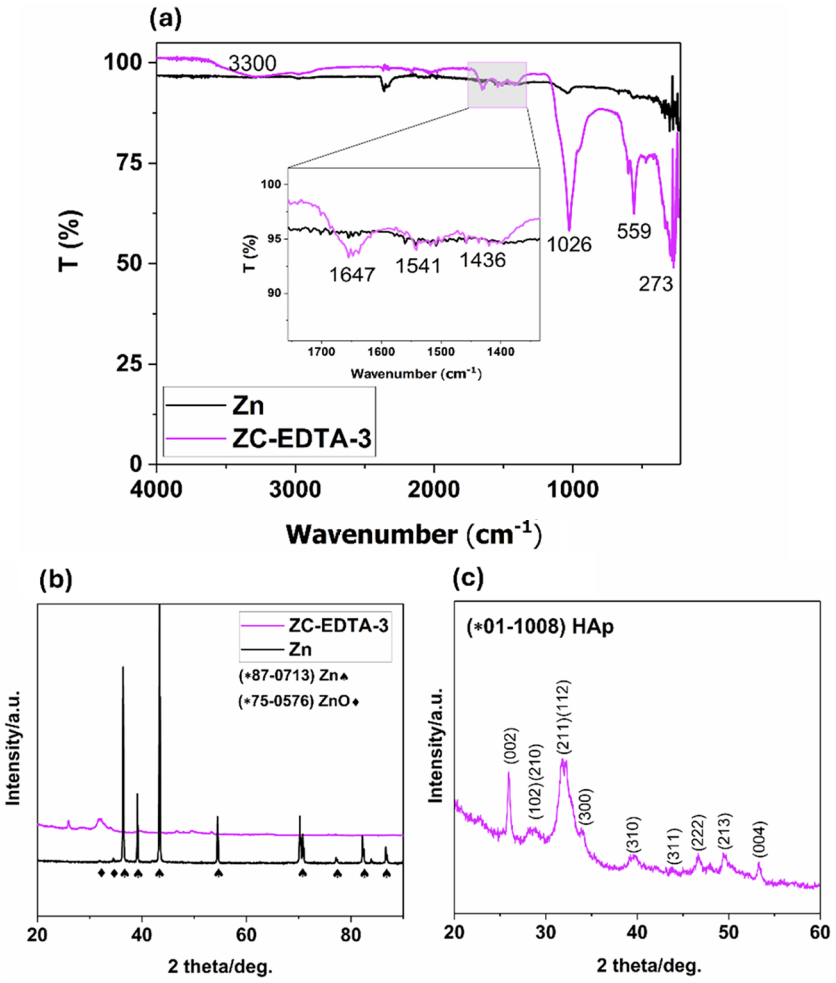

Figure 5. FTIR analysis of the optimized zinc-ceramic sample (ZC-EDTA-3) versus pure zinc substrate (a). XRD phase composition analysis of pure zinc and optimized zinc-ceramic sample (ZC-EDTA-3) (b) with the detail of 20−60 theta/deg. region (c).

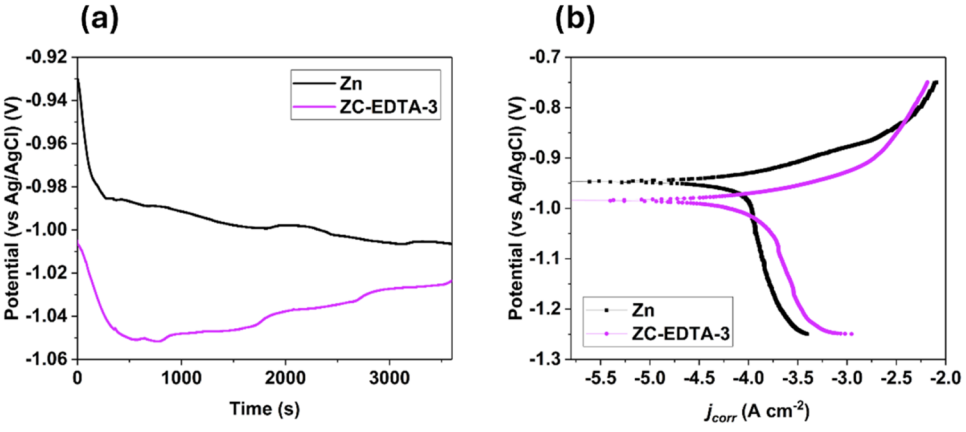

Figure 6. Potentiodynamic curves obtained from measurements in Hank's solution at 37 °C (a) with the OCP determination (b).

broad band of lower intensity located around 3300 cm^{-1} confirms the presence of the vibrational and stretching modes of the hydroxyl group (OH^-). The bands between 1436 and 1540 cm^{-1} are characteristic of the CO_3^{2-} carbonate group. The adsorbed water molecules were identified by the bands that occurred around 1647 and 1661 cm^{-1}.[60]

3.4. Phase Distribution. X-ray diffraction patterns of the ZC-EDTA-3 sample versus pure zinc substrate are displayed in Figure 5b,c. Peaks observed at (002), (102), (210), (211), (112), (300), (310), (311), (222), (213), and (004) reflections correspond to the JCPDS (card No. 01−1008). Besides that, intensive peaks for pure zinc (card No. 87−0713) and zinc oxide (card No. 75−0576) were present in the substrate.

3.5. Degradation under Physiological Conditions. Figure 6a displays the open circuit potential (OCP) development over 60 min for bare zinc and hydroxyapatite ceramic-coated zinc (ZC-EDTA-3) in a Hank's solution. The steep

https://doi.org/10.1021/acsomega.5c08241
ACS Omega 2026, 11, 1062−1076

drop in the potential at the beginning of the measurement can be seen in both samples. The ceramic coating deposition led to a more negative initial potential of the ZC-EDTA-3 sample, which started to increase after approximately 15 min of immersion. In the case of pure Zn, OCP values remained stable after the initial drop. Figure 6b presents the PDP curves, showing a clear shift in the corrosion potential (E_{corr}) for the ZC-EDTA-3 sample compared to that of bare Zn. The ZC-EDTA-3 exhibits a more negative corrosion potential and lower current density in the anodic region, indicating improved corrosion resistance due to the protective ceramic coating.

Table 3 summarizes key electrochemical parameters obtained from potentiodynamic polarization (PDP) measurements for Zn and ZC-EDTA-3 samples. The corrosion potential (E_{corr}) of the coated sample is slightly more negative (−0.984 V) than that of bare zinc (−0.947 V), indicating a minor shift in the thermodynamic tendency for corrosion. The corrosion current density (j_{corr}) decreased from $4.04 \cdot 10^{-5}$ A·cm^{-2} for Zn to 2.97×10^{-5} A·cm^{-2} for ZC-EDTA-3, reflecting a reduction in the corrosion rate. This trend correlates with the calculated corrosion rates, which decline from 0.66 mmpy for bare Zn to 0.48 mmpy for the coated sample. On the contrary, the polarization resistance of the ZC-EDTA-3 sample (252.03 Ω) is slightly lower than that of bare zinc (289.46 Ω).

Table 3. Electrochemical Parameters Obtained from the PDP Measurements for Pure Zinc and ZC-EDTA-3 Optimized Sample

	Zn	ZC-EDTA-3
E_{corr} (vs Ag/AgCl) (V)	−0.947	−0.984
j_{corr} (A·cm^{-2})	$4.04 \cdot 10^{-5}$	$2.97 \cdot 10^{-5}$
corrosion rate (mmpy)	0.66	0.48
polarization resistance (Ω)	289.46	252.03
anodic tafel slope β_a (mV/dec)	39.9	27.2
cathodic tafel slope β_c (mV/dec)	82.9	46.9

3.6. Friction Test. The friction test results shown in Figure 7 characterize the wear behavior and coefficient of friction (*CoF*) for the ZC-EDTA-3 coating and the uncoated Zn substrate. The ZC-EDTA-3 sample demonstrates a well-defined running-in phase during the initial ∼25 cycles, as evidenced by the wear depth profile in Figure 7a. In contrast, the Zn substrate exhibits a two-stage running-in process: an initial reduction in wear depth over the first ∼20 cycles followed by a pronounced increase in wear over the subsequent 60 cycles, indicating a transition to accelerated material degradation.

Notably, the Zn substrate exhibited an atypical "negative wear" phenomenon, which will be addressed in detail in the following discussion. The coefficient of friction (*CoF*) profile for the Zn sample shows a marked increase during the initial 40 cycles, indicative of complex interfacial processes associated with the onset and subsequent removal of material transfer layers characteristic of negative wear. The continued rise in *CoF* beyond this point aligns with typical behavior observed in soft−hard contact friction systems. In contrast, the ZC-EDTA-3-coated sample demonstrated enhanced tribological stability, maintaining a relatively constant CoF and consistent wear performance throughout the steady-state regime. The evolution of the CoF aligns with the findings reported in ref 61, where a dynamic frictional response was characterized by initial transient fluctuations, manifesting as pronounced increases or decreases, followed by stabilization into a steady-state regime.

The wear trends, initially derived from ball penetration depth measurements, were further validated through optical microscopy analysis of the friction track width, consistent with methodologies reported in previous studies[62,63] as illustrated in Figure 7c,d.

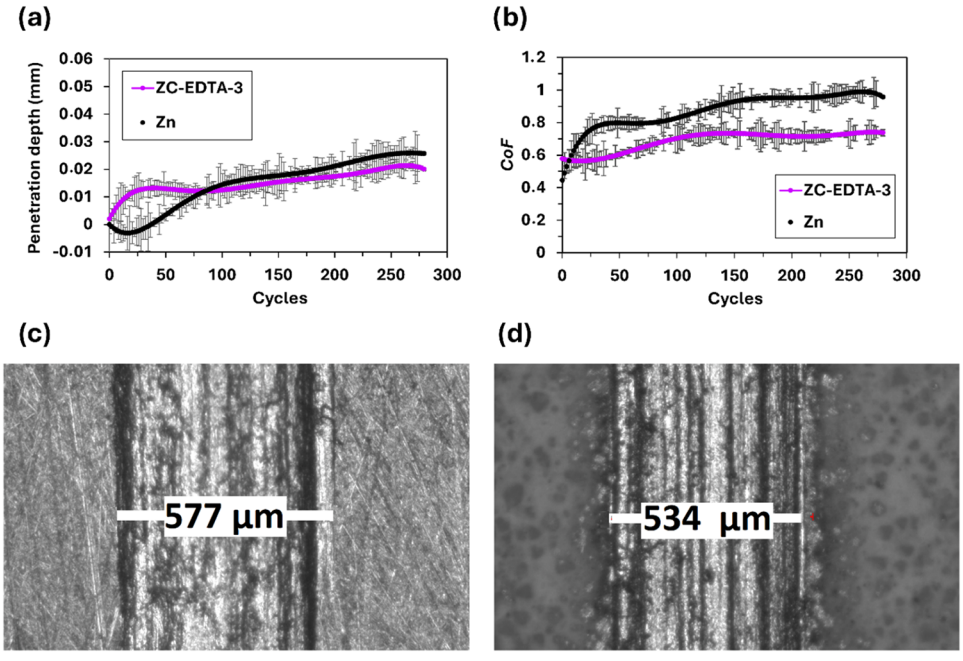

Figure 7. Variation in friction track depth over 280 sliding cycles (a). Progression of the coefficient of friction (*CoF*) (b). Representative width of the friction track: Zn substrate (c) and ZC-EDTA-3 (d).

https://doi.org/10.1021/acsomega.5c08241
ACS Omega 2026, 11, 1062−1076

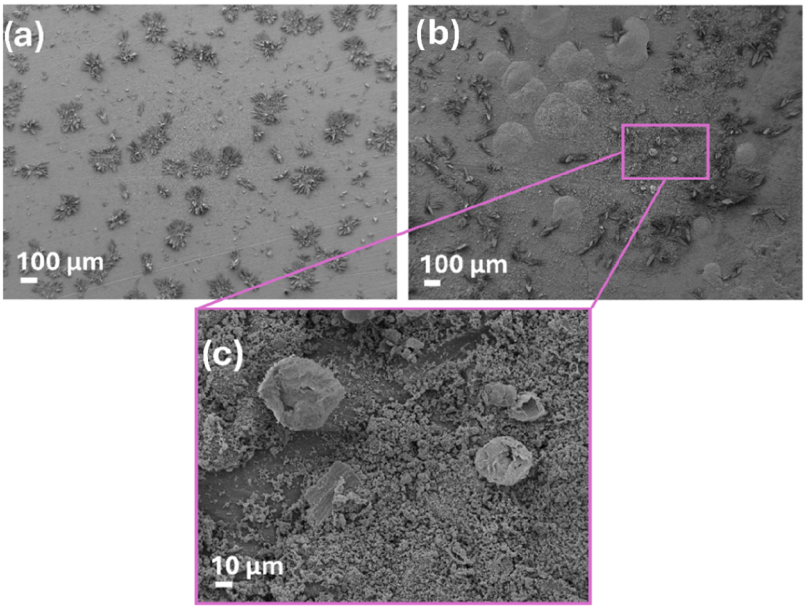

Figure 8. Platelet adhesion tests performed on pure zinc (a) and ZC-EDTA-3 optimized sample (b) with details on the adhered blood platelets (c).

3.7. Platelet Adhesion. In Figure 8, we can see representative images of the Zn and ZC-EDTA-3 surfaces of the sample after the adhesion assays of the blood platelets. After incubation of the samples in PRP, surface degradation occurred, which was manifested by the formation of crystals on the Zn sample (Figure 8a) and by the partial delamination. At the same time, there was no significant amount of adhered blood spots on the surface of both coated and uncoated samples. Isolated blood spots in small amounts were present only on the coated sample, trapped in the crystalline structure of the coating.

4. DISCUSSION

The first objective of this work was to prepare and characterize a zinc (Zn) substrate prepared by powder metallurgy. It is well-known that surface properties significantly influence the quality and adhesion of electrochemically deposited coatings.[64,65] Substrate surface with increased roughness may offer more nucleation sites, leading to increased adhesion, accelerated deposition time, and potentially thicker coatings.[66] Moreover, it was found that increased surface roughness ($R_a \sim 30$ nm) of zinc contributed to the enhanced inhibition of the bacterial film creation.[67] Therefore, the Zn samples were intentionally roughened to strengthen the adhesion of the hydroxyapatite coating before the electrodeposition. Chemical composition surface analysis revealed that, in addition to metallic zinc, a minor amount of zinc oxide (ZnO) was present on the surface, likely formed due to exposure to atmospheric moisture. The addition of ZnO nanotubes into the functional coatings of pure Zn studied by Lyu[68] demonstrated enhanced cell compatibility, while a similar coating proposed by Dong[69] showed increased electrochemical activity, which supports the positive effect of the presence of zinc oxide on Zn substrate.

Subsequently, the electrochemical deposition conditions were optimized. Uniform and strongly adherent coatings were achieved only for the ZC-EDTA-3 samples. In all tested cases, however, significant surface defects, linked to the hydrogen evolution, were observed on the deposited coatings across all tested samples. These defects were most pronounced in the ZC-EDTA-1 and ZC-EDTA-2 samples, where the formation of larger gas bubbles led to poor adhesion and partial delamination of the coating from the substrate. Hydrogen gas is generated at the working electrode (Zn) during the reduction of water[70]

$$2H_2O + 2e^- \leftrightarrow \uparrow H_2 + 2OH^- \quad (1)$$

The hydroxide ions produced during reaction 1 can subsequently react with dihydrogen phosphate anions (2)

$$H_2PO_4^- + OH^- \leftrightarrow H_2O + HPO_4^{2-} \quad (2)$$

which leads to the stoichiometric precipitation of brushite according to the reaction

$$Ca^{2+} + HPO_4^{2-} + 2H_2O \leftrightarrow CaHPO_4 \cdot 2H_2O \quad (3)$$

To enable successful deposition of a homogeneous coating, the hydrogen evolution process must be carefully controlled, as excessive gas formation can interfere with coating uniformity and adherence. Even though higher current densities are often associated with increased hydrogen evolution, it was found[71] that within a small range of current densities (lower than 5 mA·cm^{-2}), higher current densities promote the formation of a larger number of small bubbles. These bubbles can detach more easily from the surface of the working electrode (Zn), which was observed in our work with the ZC-EDTA-3 sample prepared under 1.25 mA·cm^{-2} conditions, unlike those in other samples prepared under lower (0.4 mA·cm^{-2}) current densities. Precise control of deposition parameters such as current density and electrolyte composition was applied to regulate hydrogen bubble formation and thereby improve coating uniformity and adhesion. This approach effectively mitigated the adverse effects of excessive gas evolution, as observed in the optimized ZC-EDTA-3 sample. In addition to electrochemical parameter control, other possible strategies reported in the literature include the incorporation of oxidizing agents such as hydrogen peroxide,[72] which can suppress hydrogen evolution, as well as the optimization of electrode surface geometry or electrolyte agitation to facilitate bubble detachment.

https://doi.org/10.1021/acsomega.5c08241
ACS Omega 2026, 11, 1062−1076

Besides the successful control of hydrogen gas bubble size affecting the layer porosity and defects, strong adhesion to the substrate was anticipated. The addition of EDTA significantly enhances the adhesion of electrochemically deposited hydroxyapatite coatings by controlling the local availability of calcium ions through chelation.[73,74] This controlled release prevents rapid precipitation and promotes uniform crystal growth directly on the substrate, resulting in a more crystalline, compact, and adherent layer. Moreover, EDTA helps stabilize the local pH and reduces the formation of gas bubbles from hydrogen evolution, both of which contribute to minimizing coating defects and delamination. However, at low current densities, the rate of water reduction and thus the generation of hydroxide ions (OH^-) is limited. Since OH^- is essential for phosphate conversion and subsequent calcium-phosphate precipitation, insufficient production can hinder the nucleation and growth of the coating, even with EDTA present. Similarly, short deposition times may not allow sufficient time for the controlled release of Ca^{2+} from the Ca-EDTA complex and for the gradual buildup of a uniform coating. As a result, coatings may be thin, poorly adherent, or incomplete despite the presence of EDTA, as observed in the case of ZC-EDTA-1 and ZC-EDTA-2 samples prepared with EDTA addition, yet at low current densities and insufficient time of deposition.

In addition to the coating porosity control and adhesion strength optimization, the morphology of the deposited layer was also studied. Smaller crystal morphologies are more likely to form at higher current densities as was also reported in ref 75. A similar effect of decreasing the particle size with increasing current density was observed by Li.[76] In the presence of EDTA, calcium ions are released in a controlled and gradual manner, which promotes uniform nucleation over the electrode surface rather than localized rapid precipitation. This favors the formation of rounded or spherical particles, which was also observed by Hentrich et al.[77] At the same time, higher current densities increase the generation of hydroxide ions (OH^-) via water reduction, which enhances the local pH and accelerates the precipitation of calcium phosphate. When paired with EDTA, this results in a favorable balance: rapid enough ion supply to drive deposition but still buffered and spatially controlled by the chelating agent. This condition supports the formation of dense, fine-grained, often spherical, or globular morphologies as the crystals have sufficient nucleation sites and a controlled environment to grow evenly. In contrast, without EDTA or at low current densities, the conditions favor anisotropic (directional) growth, leading to needle-like or spiky structures as was observed in the case of nonoptimized ZC samples. Similar morphologies of ceramic layer prepared by electrodeposition as observed in our study was reported in ref 78, where HAp was deposited onto Ti6Al4 V-based substrates at currents ranging from 1.5 to 3.5 mA. Sharp microneedles, as visible in SEMs of nonoptimized ZC samples, may be damaging to the bone cells and prevent their attachment and spreading. Therefore, spherical morphology (as observed in ZC-EDTA-3 sample) is more beneficial for bone cell growth.[79]

The chemical composition of the prepared HAp layer was also studied. The presence of zinc was confirmed in all EDS spectra of the studied samples except for ZC due to the local thickness of the layer from which the ZC sample was analyzed (Figure 4a). In all EDS spectra, peaks corresponding to calcium and phosphorus were observed, indicating the presence of calcium phosphates. However, the intensities of these peaks varied across the different samples, which was also reflected in the calculated Ca/P ratios. The highest Ca/P ratio (1.47) was recorded in sample ZC-EDTA-3. The typical stoichiometric ratio in hydroxyapatite is 1.67. A decrease in this ratio may be attributed to several factors. Since EDTA chelates calcium ions, it can alter the local calcium concentration near the electrode, potentially leading to deviations from the ideal Ca/P ratio if the release rate is not balanced with phosphate availability. This likely caused the lowered Ca/P ratio observed in samples prepared with EDTA addition (1.33, 1.33, and 1.47 for ZC-EDTA-1, ZC-EDTA-2, and ZC-EDTA-3, respectively) compared to the expected ratio of 1.67 for HAp. The low Ca/P ratio of the ZC sample (0.99) prepared without a chelating agent resembles that of the brushite phase[80] rather than HAp, whose formation is favored when calcium is deficient near the electrode. The SEM images also clearly revealed the local formation of larger, plate-like structures on the surface of the ZC-EDTA-3 sample, which most likely correspond to brushite as well. Brushite is primarily formed during the electrochemical deposition process and is subsequently converted to hydroxyapatite (HAp) through alkaline treatment in NaOH. Brushite is generally considered more resorbable than hydroxyapatite due to its higher solubility under physiological conditions,[81] which is favorable for the materials with potential to serve as biodegradable implants.

Another factor influencing the Ca/P ratio includes ionic substitutions (e.g., partial replacement of Ca^{2+} or PO_4^{3-} by foreign ions). Ionic substitutions, such as partial replacement of Ca^{2+} by foreign cations like Zn^{2+} which can incorporate into the hydroxyapatite lattice due to their similar charge but smaller ionic radius (since the ionic diameter of Zn^{2+} ion (0.074 nm) is smaller than that of Ca^{2+} ion (0.099 nm)), may occur.[82] Zinc substitution is of particular interest due to its known biological benefits, including enhanced antibacterial properties and promotion of bone regeneration.[83] Its presence may also contribute to the slightly reduced Ca/P ratio observed in the studied sample. Bigi et al.[84] reported that the presence of zinc in solution strongly inhibits the crystallization of hydroxyapatite, which can be synthesized as a unique crystalline phase only up to a zinc concentration of about 25 atom %. This behavior, which closely resembles that previously observed for magnesium, can be attributed to the incorporation of ions with significantly smaller ionic radii than calcium into the hydroxyapatite prenuclei. Their incorporation distorts the structure and induces a mismatch, thereby hindering further crystallization of HAp.

FTIR and XRD analyses were employed to confirm the chemical composition and phase structures of the samples. Zn ionic substitution can cause a decrease in the intensity of the OH band in the FTIR spectra of hydroxyapatite (HAp). When Zn^{2+} ions substitute for Ca^{2+} in the HAp lattice, this substitution leads to structural distortions, reduced crystallinity, and changes in the local environment of the hydroxyl groups. These effects can be manifested as a lower intensity of the OH stretching band in our FTIR spectra. The bands around 1440 cm^{-1} correspond to the asymmetric stretching vibrations (ν_3) of CO_3^{2-} ions. The presence of bands at the wavenumber around 1455, 1410, and 873 cm^{-1} is associated with the B-type substitution, in which CO_3^{2-} ions replace PO_4^{3-} ions. Such bands at similar values of wavenumber as observed in our spectrum were also observed in a study that analyzed natural nonstoichiometric hydroxyapatite isolated

https://doi.org/10.1021/acsomega.5c08241
ACS Omega 2026, 11, 1062−1076

from bone tissue.[85] However, in the spectral range of 870−880 cm^{-1}, the band corresponding to the HPO_4^{2-} was not found.[86] The absence of the HPO_4^{2-} band is attributed to its removal by alkaline treatment in 1 M NaOH, which promotes deprotonation of HPO_4^{2-} to PO_4^{3-} under highly basic conditions.

As described elsewhere, Zn incorporation in the apatite structure contributes to a decrease in the sample's crystallinity and particle size.[87] Based on the observed decrease in the Ca/P molar ratio and the reduction in crystallinity as evidenced by the broadening and weakening of characteristic peaks in both FTIR and XRD spectra, we hypothesize that zinc ions have been successfully incorporated into the hydroxyapatite lattice. The absence of separate Zn or ZnO phases in the XRD pattern of ZC-EDTA-3 sample indicates successful Zn incorporation into the HAp lattice, as was previously found in ref 88. It was also reported that when Zn doping amount exceeded 1 mol %, XRD peaks became broader and less intense, and the morphology of zinc-doped HAp crystals transforms to round particulates from needle-like crystals after Zn addition into the structure in ref 82. Similar results where smaller grain sizes were present in Zn-doped HAp layers were also observed in ref 89. These spectral and morphological changes are consistent with previously reported features of Zn-doped hydroxyapatite, further supporting our assumption.

To evaluate the performance of a biodegradable material, it is necessary to know its degradation behavior. Potentiodynamic tests in Hanks' solution simulating the human body environment showed that the deposition of the HAp-containing coating led to a decrease in the corrosion rate from 0.66 mmpy for bare Zn to 0.48 mmpy after coating, as observed in several studies.[50,90−92] On the contrary, the polarization resistance of the hydroxyapatite-coated sample was lower, and the corrosion potential was more negative compared to pure Zn, which may be due to several effects. The first of these is the presence of a passivation layer formed by ZnO on pure Zn, the presence of which was also confirmed by an EDS analysis. The second factor contributing to these results is the porosity of the prepared coating. The lower polarization resistance of HAp-coated zinc, despite reduced corrosion rate (from 0.66 mmpy for Zn to 0.48 mmpy for HAp-coated sample) and current density, is likely due to porosity or defects in the coating and differences in interfacial behavior compared to those of the passive film formed on uncoated Zn. Material density plays an important role in the corrosion behavior of metals. Higher-density materials tend to exhibit lower corrosion rates. The density of the substrate material (Zn) used in this paper was previously studied in our previous work.[93] In the study of Shoeib,[70] studying the electrochemical performance of zinc-HAp and zinc-brushite materials prepared by electrodeposition and microwave-assisted route was found that the corrosion potential of untreated zinc vs HAp treated sample was −1.07 and −1.05 A, respectively, while the corresponding corrosion rates were 0.41 (Zn) and 0.30 mmpy (Zn-HAp). Similarly, as in our study, deposition of the HAp layer led to the decrease in the corrosion rate; however, a less dense and more porous structure in our case led to the higher corrosion rates of the coated samples (0.48 mmpy). Although the initial tests conducted in Hanks' solution provided preliminary insights into the material's behavior, further investigations under more complex conditions, such as in protein-containing environments and *in vivo*, are required.

Besides the degradation behavior, assessing the wear resistance of hydroxyapatite coatings on biodegradable zinc substrates is vital for advancing next-generation bioimplants. This study employs a ball counter body made of stainless steel, whose superior hardness minimizes reciprocal wear, enabling accurate analysis of the coating's durability. The wear process of a frictional contact pair typically progresses through three distinct stages: running-in phase, steady-state wear, and accelerated wear. The running-in stage, governed by complex mechanical, physical, and chemical interactions, plays a pivotal role in determining the overall wear resistance of the components. By the end of this period, key surface characteristics such as roughness, microhardness, residual stress distribution, subsurface structure, and surface integrity reach optimal values tailored to the prevailing operating conditions.[94] Observation of "negative wear" in metals is confusing since the wear typically implies material loss. Conversely, in certain cases, a phenomenon resembling negative wear can arise from the material transfer. Rather than material loss, the metal surface can experience a gain when a softer metal abrades a harder one, leading to the adhesion of particles (debris) from the harder surface to the softer one. Another possibility is the formation of oxide layers or tribofilms that build up on the surface. These layers can temporarily increase the apparent volume of the friction track. From a tribological perspective, the presence of a hydroxyapatite film appears to have a negative effect on the zinc substrate due to its seemingly increased wear rate at the beginning of the test. However, this elevated wear is not indicative of material loss but rather reflects the coating's protective function in preventing undesirable material transfer. This behavior is attributed to the pronounced hardness mismatch between HAp (4−5 GPa)[95] and Zn (0.3−0.4 GPa).[96] During sliding contact, HAp provides a degree of protection to the underlying substrate. This is achieved by stabilizing the wear process and mitigating the negative wear artifacts as in the case of uncoated Zn surfaces. Thus, the ZC-EDTA-3 coating demonstrated pronounced protective behavior, effectively preserving surface integrity throughout the test and reflecting superior mechanical and tribological performance. Quantitative analysis of the friction track widths revealed values of approximately 530 μm for ZC-EDTA-3 and ∼580 μm for the uncoated Zn substrate (Figure 7c,d). The previously discussed assumptions are indirectly validated by the observed *CoF* values. This behavior highlights the improved tribological performance of the coated systems, likely due to enhanced mechanical integrity, surface conformity, and resistance to interfacial degradation. The trend of a gradual increase in *CoF* values of the Zn substrate is commonly associated with evolving surface conditions such as the accumulation of wear debris, oxidation, or tribochemical reactions exacerbated by friction-induced heating. Additionally, as the running-in phase completes, the transition to steady-state wear leads to further surface roughening and increased frictional resistance. Generally, the findings indicate that the application of hydroxyapatite coatings plays an important role in enhancing surface performance.

The last parameter observed on the optimized ZC-EDTA-3 surface was its potential thrombogenicity, which was studied by observing the morphology and the rates of occurrence of adhered blood platelets on the coated and bare Zn surface. In the case of pure Zn, no adhered blood spots were observed on the surface of the samples, whereas in the case of the HAp-coated sample, solitary spherical spots could be observed.

https://doi.org/10.1021/acsomega.5c08241
ACS Omega 2026, 11, 1062−1076

Platelets were observed at sites of increased heterogeneity and roughness on the surface of the ZC-EDTA-3 samples. The flattened oval shape with no pseudopodia present suggests that only inactive platelets remained trapped on the coating. These results are in line with the results previously studied on HAp-coated metallic surfaces. Although we have obtained preliminary results indicating the basic thrombogenic properties of the material, its successful implementation in practice will require further biological testing in the future, specifically focusing on the cytotoxicity of the material by using different cell lines.

CONCLUSIONS

The main objective of the present study was to optimize the process of electrochemical deposition of the ceramic layer on Zn substrate to prepare new materials with the potential to serve as degradable implants in bone repair applications. The hydroxyapatite ceramic coating was chosen due to its effect on reducing the corrosion rate of the zinc substrate and also due to its significant biological role in the process of formation of new bone tissue. Hydroxyapatite (HAp) coatings were successfully obtained, with the best performance observed at 120 min deposition time, a current density of 1.25 $mA{\cdot}cm^{-2}$, and the addition of EDTA-2Na as a chelating agent. EDTA affects the electrochemical deposition of HAp not only by improving adhesion and morphology but also by enabling better crystallinity, closer-to-ideal stoichiometric Ca/P ratios, and higher phase purity. The chemical and phase compositions of the deposited coating indicate the presence of Zn-doped hydroxypatite, while the source of the Zn is the substrate itself, releasing zinc ions during its dissolution into solution. These HAp coatings also regulate frictional responses under mechanical loading and significantly reduce the extent of wear-induced deterioration observed in untreated zinc substrates. Future experiments should therefore aim at comprehensive biological evaluation, including *in vitro* and *in vivo* studies, to validate the biocompatibility and osteogenic potential of the coatings. In addition, further work should focus on controlling coating porosity and minimizing interfacial defects as these factors remain critical for long-term stability and reliable implant performance.

AUTHOR INFORMATION

Corresponding Author

Radka Gorejova − *Department of Physical Chemistry, Faculty of Science, Pavol Jozef Šafárik University in Košice, 041 54 Košice, Slovakia;* orcid.org/0000-0002-7892-7581; Email: radka.gorejova@upjs.sk

Authors

Ivana Mojzisova − *Department of Physical Chemistry, Faculty of Science, Pavol Jozef Šafárik University in Košice, 041 54 Košice, Slovakia*

Evghenii Harea − *Centre of Polymer Systems, University Institute, Tomas Bata University in Zlín, 76001 Zlín, Czech Republic;* orcid.org/0000-0001-5008-1062

Tibor Sopcak − *Institute of Materials Research, Slovak Academy of Sciences, 040 01 Košice, Slovakia;* orcid.org/0000-0003-1818-8358

Kadir Ozaltin − *Centre of Polymer Systems, University Institute, Tomas Bata University in Zlín, 76001 Zlín, Czech Republic;* orcid.org/0000-0002-7619-5321

Complete contact information is available at: https://pubs.acs.org/10.1021/acsomega.5c08241

Author Contributions

R.G. Conceptualization, methodology, investigation, funding acquisition, and writing−original draft; I.M. Investigation, validation, and formal analysis; E.H. Investigation, formal analysis, and writing−original draft; T.S. Investigation and formal analysis; and K.O. Investigation, formal analysis, and writing−review and editing.

Notes

The authors declare no competing financial interest.

ACKNOWLEDGMENTS

This work was funded by the EU NextGenerationEU through the Recovery and Resilience Plan for Slovakia under project ZETA no. 09I03-03-V04-00010.

REFERENCES

(1) Nouri, A.; Shirvan, A. R.; Li, Y.; Wen, C. Biodegradable Metallic Suture Anchors: A Review. *Smart Mater. Manuf.* **2023**, *1*, No. 100005.

(2) Zhang, J.; Jiang, Y.; Shang, Z.; Zhao, B.; Jiao, M.; Liu, W.; Cheng, M.; Zhai, B.; Guo, Y.; Liu, B.; Shi, X.; Ma, B. Biodegradable Metals for Bone Defect Repair: A Systematic Review and Meta-Analysis Based on Animal Studies. *Bioact. Mater.* **2021**, *6* (11), 4027−4052.

(3) Xia, D.; Yang, F.; Zheng, Y.; Liu, Y.; Zhou, Y. Research Status of Biodegradable Metals Designed for Oral and Maxillofacial Applications: A Review. *Bioact. Mater.* **2021**, *6* (11), 4186−4208.

(4) Asgari, M.; Hang, R.; Wang, C.; Yu, Z.; Li, Z.; Xiao, Y. Biodegradable Metallicwires in Dental and Orthopedic Applications: A Review. *Metals* **2018**, *8* (4), No. 212.

(5) Wei, S.; Ma, J. X.; Xu, L.; Gu, X. S.; Ma, X. L. Biodegradable Materials for Bone Defect Repair. *Mil. Med. Res.* **2020**, *7* (1), No. 54.

(6) Sheikh, Z.; Najeeb, S.; Khurshid, Z.; Verma, V.; Rashid, H.; Glogauer, M. Biodegradable Materials for Bone Repair and Tissue Engineering Applications. *Materials* **2015**, *8* (9), 5744−5794.

(7) Wang, P.; Gong, Y.; Zhou, G.; Ren, W.; Wang, X. Biodegradable Implants for Internal Fixation of Fractures and Accelerated Bone Regeneration. *ACS Omega* **2023**, *8* (31), 27920−27931.

(8) Zivic, F.; Grujovic, N.; Pellicer, E.; Sort, J.; Mirovic, S.; Adamovic, D.; Vulovic, M. Biodegradable Metals as Biomaterials for Clinical Practice: Iron-Based Materials. In *Biomaterials in Clinical Practice*; Springer: Cham, 2017; p 225.

(9) Wegener, B.; Sichler, A.; Milz, S.; Sprecher, C.; Pieper, K.; Hermanns, W.; Jansson, V.; Nies, B.; Kieback, B.; Müller, P. E.; Wegener, V.; Quadbeck, P. Development of a Novel Biodegradable Porous Iron-Based Implant for Bone Replacement. *Sci. Rep.* **2020**, *10* (1), No. 9141.

(10) Gąsior, G.; Szczepański, J.; Radtke, A. Biodegradable Iron-Based Materials—What Was Done and What More Can Be Done? *Materials* **2021**, *14* (12), No. 3381.

(11) Li, Y.; Jahr, H.; Lietaert, K.; Pavanram, P.; Yilmaz, A.; Fockaert, L. I.; Leeflang, M. A.; Pouran, B.; Gonzalez-Garcia, Y.; Weinans, H.; Mol, J. M. C.; Zhou, J.; Zadpoor, A. A. Additively Manufactured Biodegradable Porous Iron. *Acta Biomater.* **2018**, *77*, 380−393.

(12) Salama, M.; Maria, F.; Santos, C.; et al. Biodegradable Iron and Porous Iron: Mechanical Properties, Degradation Behaviour, Manufacturing Routes and Biomedical Applications. *J. Funct. Biomater.* **2022**, *13* (2), No. 72.

(13) Sezer, N.; Evis, Z.; Kayhan, S. M.; Tahmasebifar, A.; Koç, M. Review of Magnesium-Based Biomaterials and Their Applications. *J. Magn. Alloys* **2018**, *6* (1), 23−43.

(14) Wang, J. L.; Xu, J. K.; Hopkins, C.; Chow, D. H. K.; Qin, L. Biodegradable Magnesium-Based Implants in Orthopedics—A General Review and Perspectives. *Adv. Sci.* **2020**, *7* (8), No. 1902443, DOI: 10.1002/advs.201902443.

(15) Li, Y.; Zhou, J.; Pavanram, P.; Leeflang, M. A.; Fockaert, L. I.; Pouran, B.; Tümer, N.; Schröder, K. U.; Mol, J. M. C.; Weinans, H.; Jahr, H.; Zadpoor, A. A. Additively Manufactured Biodegradable Porous Magnesium. *Acta Biomater.* **2018**, *67*, 378−392.
(16) Banerjee, P. C.; Al-Saadi, S.; Choudhary, L.; Harandi, S. E.; Singh, R. Magnesium Implants: Prospects and Challenges. *Materials* **2019**, *12* (1), No. 136.
(17) Liu, S.; Gao, M.; Liu, N.; Li, R.; Zhang, Z.; Yao, Y.; Wang, W.; Tan, L.; Zhang, N. Osteoinduction and Osteoconduction Evaluation of Biodegradable Magnesium Alloy Scaffolds in Repairing Large Segmental Defects in Long Bones of Rabbit Models. *ACS Omega* **2024**, *9* (46), 46419−46428.
(18) Wu, W.; Wang, Z.; Zang, S.; Yu, X.; Yang, H.; Chang, S. Research Progress on Surface Treatments of Biodegradable Mg Alloys: A Review. *ACS Omega* **2020**, *5* (2), 941−947.
(19) Su, Y.; Cockerill, I.; Wang, Y.; Qin, Y. X.; Chang, L.; Zheng, Y.; Zhu, D. Zinc-Based Biomaterials for Regeneration and Therapy. *Trends Biotechnol.* **2019**, *37* (4), 428−441.
(20) Pospíšilová, I.; Vojtěch, D. Zinc Alloys for Biodegradable Medical Implants. *Mater. Sci. Forum* **2014**, *782*, 457−460.
(21) Li, Y.; Pavanram, P.; Zhou, J.; Lietaert, K.; Bobbert, F. S. L.; Kubo, Y.; Leeflang, M. A.; Jahr, H.; Zadpoor, A. A. Additively Manufactured Functionally Graded Biodegradable Porous Zinc. *Biomater. Sci.* **2020**, *8*, 646−661.
(22) Bowen, P. K.; Drelich, J.; Goldman, J. Zinc Exhibits Ideal Physiological Corrosion Behavior for Bioabsorbable Stents. *Adv. Mater.* **2013**, *25* (18), 2577−2582.
(23) Li, Y.; Li, W.; Bobbert, F. S. L.; Lietaert, K.; Dong, J. H.; Leeflang, M. A.; Zhou, J.; Zadpoor, A. A. Corrosion Fatigue Behavior of Additively Manufactured Biodegradable Porous Zinc. *Acta Biomater.* **2020**, *106*, 439−449.
(24) Törne, K.; Larsson, M.; Norlin, A.; Weissenrieder, J. Degradation of Zinc in Saline Solutions, Plasma, and Whole Blood. *J. Biomed. Mater. Res., Part B* **2016**, *104* (6), 1141−1151.
(25) Levy, G. K.; Goldman, J.; Aghion, E. The Prospects of Zinc as a Structural Material for Biodegradable Implants—a Review Paper. *Metals* **2017**, *7* (10), No. 402.
(26) Peng, K.; Qiao, A.; Ohta, M.; Putra, N. K.; Cui, X.; Mu, Y.; Anzai, H. Structural Design and Numerical Analysis of a Novel Biodegradable Zinc Alloy Stent. *Comput. Model. Eng. Sci.* **2018**, *117* (1), 17−28.
(27) Vojtěch, D.; Kubásek, J.; Čapek, J.; Pospíšilová, I. Comparative Mechanical and Corrosion Studies on Magnesium, Zinc and Iron Alloys as Biodegradable Metals. *Mater. Tehnol.* **2015**, *49* (6), 877−882.
(28) Nikody, M.; Li, J.; Balmayor, E. R.; Moroni, L.; Habibovic, P. The Addition of Zinc Ions to Polymer-Ceramic Composites Accelerated Osteogenic Differentiation of Human Mesenchymal Stromal Cells. *Biomater. Adv.* **2023**, *149*, No. 213391.
(29) Vijayakumar, G.; Sundaram, G. A.; Mani, S. P.; Kumar, S. P.; Krishnan, M.; Lakshmanan, S. Strontium and Zinc Doped Hydroxyapatite Coating on Stainless Steel Mini-implants Used in Maxillofacial Surgery: An in-Vitro Study. *Library Prog. Int.* **2024**, *44* (3), 1846−1852.
(30) Shahed, C. A.; Ahmad, F.; Günister, E.; Foudzi, F. M.; Ali, S.; Malik, K.; Harun, W. S. W. Antibacterial Mechanism with Consequent Cytotoxicity of Different Reinforcements in Biodegradable Magnesium and Zinc Alloys: A Review. *J. Magn. Alloys* **2023**, *11* (9), 3038−3058.
(31) Liu, Q.; Li, A.; Liu, S.; Fu, Q.; Xu, Y.; Dai, J.; Li, P.; Xu, S. Cytotoxicity of Biodegradable Zinc and Its Alloys: A Systematic Review. *J. Funct. Biomater.* **2023**, *14* (4), No. 206.
(32) Cuypers, L. A. B.; Bertsch, P.; Wang, R.; Harhangi, H. R.; Joziasse, L. S.; Walboomers, X. F.; van Niftrik, L.; Yang, F.; Leeuwenburgh, S. C. G. The Effect of Zinc Doping on the Cytocompatibility and Antibacterial Efficacy of Hydroxyapatite Nanoparticles for Treatment of Bone Infection. *Open Ceram.* **2023**, *16*, No. 100488, DOI: 10.1016/j.oceram.2023.100488.
(33) Wang, Y.; Zhai, W.; Cheng, S.; Li, J.; Zhang, H. Surface-Functionalized Design of Blood-Contacting Biomaterials for Preventing Coagulation and Promoting Hemostasis. *Friction* **2023**, *11* (8), 1371−1394.
(34) Zhang, S.; Zhang, X.; Zhao, C.; Li, J.; Song, Y.; Xie, C.; Tao, H.; Zhang, Y.; He, Y.; Jiang, Y.; Bian, Y. Research on an Mg-Zn Alloy as a Degradable Biomaterial. *Acta Biomater.* **2010**, *6* (2), 626−640.
(35) Kubásek, J.; Dvorský, D.; Čapek, J.; Pinc, J.; Vojtěch, D. Zn-Mg Biodegradable Composite: Novel Material with Tailored Mechanical and Corrosion Properties. *Materials* **2019**, *12* (23), No. 3930.
(36) Gong, H.; Wang, K.; Strich, R.; Zhou, J. G. In Vitro Biodegradation Behavior, Mechanical Properties, and Cytotoxicity of Biodegradable Zn-Mg Alloy. *J. Biomed. Mater. Res., Part B* **2015**, *103* (8), 1632−1640.
(37) Miao, H.; Zhang, D.; Chen, C.; Zhang, L.; Pei, J.; Su, Y.; Huang, H.; Wang, Z.; Kang, B.; Ding, W.; Zeng, H.; Yuan, G. Research on Biodegradable Mg-Zn-Gd Alloys for Potential Orthopedic Implants: In Vitro and in Vivo Evaluations. *ACS Biomater. Sci. Eng.* **2019**, *5* (3), 1623−1634.
(38) Wang, H.; Zhu, S.; Wang, L.; Feng, Y.; Ma, X.; Guan, S. Formation Mechanism of Ca-Deficient Hydroxyapatite Coating on Mg-Zn-Ca Alloy for Orthopaedic Implant. *Appl. Surf. Sci.* **2014**, *307*, 92−100.
(39) Hänzi, A. C.; Gerber, I.; Schinhammer, M.; Löffler, J. F.; Uggowitzer, P. J. On the in Vitro and in Vivo Degradation Performance and Biological Response of New Biodegradable Mg-Y-Zn Alloys. *Acta Biomater.* **2010**, *6* (5), 1824−1833.
(40) Shi, Y.; Xue, Z.; Li, P.; Yang, S.; Zhang, D.; Zhou, S.; Guan, Z.; Li, Y.; Wang, L. N. Surface Modification on Biodegradable Zinc Alloys. *J. Mater. Res. Technol.* **2023**, *25*, 3670−3687.
(41) Safavi, M. S.; Walsh, F. C.; Surmeneva, M. A.; Surmenev, R. A.; Khalil-Allafi, J. Electrodeposited Hydroxyapatite-Based Biocoatings: Recent Progress and Future Challenges. *Coatings* **2021**, *11* (1), No. 110.
(42) Harun, W. S. W.; Asri, R. I. M.; Alias, J.; Zulkifli, F. H.; Kadirgama, K.; Ghani, S. A. C.; Shariffuddin, J. H. M. A Comprehensive Review of Hydroxyapatite-Based Coatings Adhesion on Metallic Biomaterials. *Ceram. Int.* **2018**, *44* (2), 1250−1268.
(43) El-Habashy, S. E.; Eltaher, H. M.; Gaballah, A.; Zaki, E. I.; Mehanna, R. A.; El-Kamel, A. H. Hybrid Bioactive Hydroxyapatite/Polycaprolactone Nanoparticles for Enhanced Osteogenesis. *Mater. Sci. Eng., C* **2021**, *119*, No. 111599.
(44) Asri, R. I. M.; Harun, W. S. W.; Hassan, M. A.; Ghani, S. A. C.; Buyong, Z. A Review of Hydroxyapatite-Based Coating Techniques: Sol-Gel and Electrochemical Depositions on Biocompatible Metals. *J. Mech. Behav. Biomed. Mater.* **2016**, *57*, 95−108.
(45) Li, T. T.; Ling, L.; Lin, M. C.; Peng, H. K.; Ren, H. T.; Lou, C. W.; Lin, J. H. Recent Advances in Multifunctional Hydroxyapatite Coating by Electrochemical Deposition. *J. Mater. Sci.* **2020**, *55*, 6352−6374.
(46) Venkatesan, J.; Kim, S. K. Nano-Hydroxyapatite Composite Biomaterials for Bone Tissue Engineering - A Review. *J. Biomed. Nanotechnol.* **2014**, *10*, 3124−3140.
(47) Kattimani, V. S.; Kondaka, S.; Lingamaneni, K. P. Hydroxyapatite−-Past, Present, and Future in Bone Regeneration. *Bone Tissue Regener. Insights* **2016**, *7*, 9−19.
(48) Vijayakumar, G.; Sundaram, G. A.; Mani, S. P.; Kumar, S. P.; Krishnan, M.; Lakshmanan, S. Strontium and Zinc Doped Hydroxyapatite Coating on Stainless Steel Mini-Implants Used in Maxillofacial Surgery: An in-Vitro Study. *Library Prog. Int.* **2024**, *44*, 1846−1852.
(49) Deligianni, D. D.; Katsala, N. D.; Koutsoukos, P. G.; Missirlis, Y. F. Effect of Surface Roughness of Hydroxyapatite on Human Bone Marrow Cell Adhesion, Proliferation, Differentiation and Detachment Strength. *Biomaterials* **2000**, *22*, 87−96.
(50) Jamesh, M.; Kumar, S.; Narayanan, T. S. N. S. Electrodeposition of Hydroxyapatite Coating on Magnesium for Biomedical Applications. *J. Coat. Technol. Res.* **2012**, *9* (4), 495−502.

(51) Thanh, D. T. M.; Nam, P. T.; Phuong, N. T.; Que, L. X.; Van Anh, N.; Hoang, T.; Lam, T. D. Controlling the Electrodeposition, Morphology and Structure of Hydroxyapatite Coating on 316L Stainless Steel. *Mater. Sci. Eng., C* **2013**, *33* (4), 2037−2045.
(52) Song, Y. W.; Shan, D. Y.; Han, E. H. Electrodeposition of Hydroxyapatite Coating on AZ91D Magnesium Alloy for Biomaterial Application. *Mater. Lett.* **2008**, *62* (17−18), 3276−3279.
(53) Bakhsheshi-Rad, H. R.; Hamzah, E.; Ismail, A. F.; Aziz, M.; Daroonparvar, M.; Saebnoori, E.; Chami, A. In Vitro Degradation Behavior, Antibacterial Activity and Cytotoxicity of TiO2-MAO/ZnHA Composite Coating on Mg Alloy for Orthopedic Implants. *Surf. Coat. Technol.* **2018**, *334*, 450−460.
(54) Zielinski, A.; Bartmanski, M. Electrodeposited Biocoatings, Their Properties and Fabrication Technologies: A Review. *Coatings* **2020**, *10* (8), No. 782.
(55) Kumar, M.; Dasarathy, H.; Riley, C. Electrodeposition of Brushite Coatings and Their Transformation to Hydroxyapatite in Aqueous Solutions. *J. Biomed. Mater. Res.* **1999**, *45* (4), 302−310.
(56) Song, Y.; Zhang, S.; Li, J.; Zhao, C.; Zhang, X. Electrodeposition of Ca-P Coatings on Biodegradable Mg Alloy: In Vitro Biomineralization Behavior. *Acta Biomater.* **2010**, *6* (5), 1736−1742.
(57) Thangaraj, V. Electrodeposition and Corrosion Behaviour of Some Zn-Fe Group Metal Alloys by Pulsed Current. *Trans. IMF* **2009**, *87* (4), 208−216.
(58) Dev, P. R.; Anand, C. P.; Michael, D. S.; Wilson, P. Hydroxyapatite Coatings: A Critical Review on Electrodeposition Parametric Variations Influencing Crystal Facet Orientation towards Enhanced Electrochemical Sensing. *Mater. Adv.* **2022**, *3*, 7773−7809.
(59) Harea, E.; Lapsker, I.; Laikhtman, A.; Rapoport, L. Bauschinger's Effect and Dislocation Structure under Friction of LiF Single Crystals. *Tribol. Lett.* **2013**, *52* (2), 205−212.
(60) Hamza, M.; Kanwal, Q.; Ali, Z.; Zargar, S.; Alshammari, A. H.; Wani, T. A.; Rizwan, M.; Rohm, K.; Mushtaq, M. A. Exploring the Molecular Biology of Zinc-Doped Hydroxyapatite Nanocomposites as Fillers for Dental Materials: A Self-Defensive Approach Targeting Bacterial DNA. *Mater. Res. Express* **2024**, *11* (9), No. 095401, DOI: 10.1088/2053-1591/ad7785.
(61) Osafo, S. A.; Asumadu, T.; Klenam, D.; Etinosa, P.; Obayemi, J. D.; Agyei-Tuffour, B.; Yaya, A.; Dodoo-Arhin, D.; Eluu, S. C.; Soboyejo, W. Tribological Properties of Hydroxyapatite-Coated Nanorods on Ti-6Al-4V Surfaces. *Sci. Rep.* **2025**, *15* (1), No. 19113, DOI: 10.1038/s41598-025-03253-8.
(62) Harea, E.; Stoček, R.; Machovský, M. Study of Friction and Wear of Thermoplastic Vulcanizates: The Correlation with Abraded Surfaces Topology. *J. Phys.: Conf. Ser.* **2017**, *843* (1), No. 012070.
(63) Harea, E.; Stoček, R.; Storozhuk, L.; Sementsov, Y.; Kartel, N. Study of Tribological Properties of Natural Rubber Containing Carbon Nanotubes and Carbon Black as Hybrid Fillers. *Appl. Nanosci.* **2019**, *9*, 899−906.
(64) Góral, A.; Lityńska-Dobrzyńska, L.; Kot, M. Effect of Surface Roughness and Structure Features on Tribological Properties of Electrodeposited Nanocrystalline Ni and Ni/Al2O3 Coatings. *J. Mater. Eng. Perform.* **2017**, *26* (5), 2118−2128.
(65) Zhang, H.; Liu, Y.; Yuan, J.; Zhu, M.; Chen, J.; Wang, Z. The Influence of Substrate Surface Treatment on the Electrodeposition of (Co,Mn)3O4spinel Precursor Coatings. *Mater. Res. Express* **2020**, *7* (7), No. 076405.
(66) Ahmadian, H.; Zhou, T.; Guo, W.; Yu, Q.; Sadoun, A. M.; Fathy, A.; Xuanzhe, Y.; Elmahdy, M. Influence of Initial Surface Roughness on the Deposition and Adhesion of Electroless Ni-P Plating on 6H-SiC Substrate. *Results Eng.* **2025**, *25*, No. 103891.
(67) Xiang, E.; Moran, C. S.; Ivanovski, S.; Abdal-hay, A. Nanosurface Texturing for Enhancing the Antibacterial Effect of Biodegradable Metal Zinc: Surface Modifications. *Nanomaterials* **2023**, *13* (13), No. 2022.
(68) Lyu, H.; He, Z.; Chan, Y. K.; He, X.; Yu, Y.; Deng, Y. Hierarchical ZnO Nanotube/Graphene Oxide Nanostructures Endow Pure Zn Implant with Synergistic Bactericidal Activity and Osteogenicity. *Ind. Eng. Chem. Res.* **2019**, *58* (42), 19377−19385.
(69) Dong, H.; Zhou, J.; Virtanen, S. Fabrication of ZnO Nanotube Layer on Zn and Evaluation of Corrosion Behavior and Bioactivity in View of Biodegradable Applications. *Appl. Surf. Sci.* **2019**, *494*, 259−265.
(70) Shoeib, M. A.; Abdel-Gawad, S. A. High Performance Nano Hydroxyapatite Coating on Zinc for Biomedical Applications. *J. Mater. Sci.* **2023**, *58* (2), 740−756.
(71) Jiménez, C.; Talavera, B.; Sáez, C.; Cañizares, P.; Rodrigo, M. A. Study of the Production of Hydrogen Bubbles at Low Current Densities for Electroflotation Processes. *J. Chem. Technol. Biotechnol.* **2010**, *85* (10), 1368−1373.
(72) Ling, L.; Li, T. T.; Lin, M. C.; Jiang, Q.; Ren, H. T.; Lou, C. W.; Lin, J. H. Effect of Hydrogen Peroxide Concentration on the Nanostructure of Hydroxyapatite Coatings via Ultrasonic-Assisted Electrodeposition. *Mater. Lett.* **2020**, *261*, No. 126989, DOI: 10.1016/j.matlet.2019.126989.
(73) He, D.; Du, J.; Liu, P.; Liu, X.; Chen, X.; Li, W.; Zhang, K.; Ma, F. Influence of EDTA-2Na on the Hydroxyapatite Coating Deposited by Hydrothermal-Electrochemical Method on Ti6Al4V Surface. *Surf. Coat. Technol.* **2019**, *365*, 242−247.
(74) Kyrylenko, S.; Warchoł, F.; Oleshko, O.; Husak, Y.; Kazek-Kęsik, A.; Korniienko, V.; Deineka, V.; Sowa, M.; Maciej, A.; Michalska, J.; Jakóbik-Kolon, A.; Matuła, I.; Basiaga, M.; Hulubnycha, V.; Stolarczyk, A.; Pisarek, M.; Mishchenko, O.; Pogorielov, M.; Simka, W. Effects of the Sources of Calcium and Phosphorus on the Structural and Functional Properties of Ceramic Coatings on Titanium Dental Implants Produced by Plasma Electrolytic Oxidation. *Mater. Sci. Eng., C* **2021**, *119*, No. 111607.
(75) Djošić, M.; Panić, V.; Stojanović, J.; Mitrić, M.; Miskovic-Stankovic, V. B. The Effect of Applied Current Density on the Surface Morphology of Deposited Calcium Phosphate Coatings on Titanium. *Colloids Surf., A* **2012**, *400*, 36−43.
(76) Li, T. T.; Ling, L.; Lin, M. C.; Jiang, Q.; Lin, Q.; Lou, C. W.; Lin, J. H. Effects of Ultrasonic Treatment and Current Density on the Properties of Hydroxyapatite Coating via Electrodeposition and Its in Vitro Biomineralization Behavior. *Mater. Sci. Eng., C* **2019**, *105*, No. 110062.
(77) Hentrich, D.; Tauer, K.; Espanol, M.; Ginebra, M. P.; Taubert, A. EDTA and NTA Effectively Tune the Mineralization of Calcium Phosphate from Bulk Aqueous Solution. *Biomimetics* **2017**, *2* (4), No. 24.
(78) Ehlert, M.; Radtke, A.; Bartmański, M.; Piszczek, P. Evaluation of the Cathodic Electrodeposition Effectiveness of the Hydroxyapatite Layer Used in Surface Modification of Ti6Al4V-Based Biomaterials. *Materials* **2022**, *15* (19), No. 6925.
(79) Drevet, R.; Benhayoune, H. Electrodeposition of Calcium Phosphate Coatings on Metallic Substrates for Bone Implant Applications: A Review. *Coatings* **2022**, *12* (4), No. 539.
(80) Mirković, M.; Yilmaz, M. S.; Kljajević, L.; Pavlović, V.; Ivanović, M.; Djukić, D.; Eren, T. Design of PEI and Amine Modified Metakaolin-Brushite Hybrid Polymeric Composite Materials for CO2 Capturing. *Polymers* **2023**, *15* (7), No. 1669.
(81) Charrière, E.; Terrazzoni, S.; Pittet, C.; Mordasini, P.; Dutoit, M.; tre, J. L.; Zysset, P. Mechanical Characterization of Brushite and Hydroxyapatite Cements. *Biomaterials* **2001**, *22*, 2937−2945.
(82) Uysal, I.; Yilmaz, B.; Evis, Z. Zn-Doped Hydroxyapatite in Biomedical Applications. *J. Aust. Ceram. Soc.* **2021**, *57*, 869−897.
(83) Molenda, M.; Kolmas, J. The Role of Zinc in Bone Tissue Health and Regeneration—a Review. *Biol. Trace Elem. Res.* **2023**, *201* (12), 5640−5651.
(84) Bigi, A.; Foresti, E.; Gandolfi, M.; Gazzano, M.; Roveri, N. Inhibiting Effect of Zinc on Hydroxylapatite Crystallization. *J. Inorg. Biochem.* **1995**, *58*, 49−58.
(85) Gheisari, H.; Karamian, E.; Abdellahi, M. A Novel Hydroxyapatite -Hardystonite Nanocomposite Ceramic. *Ceram. Int.* **2015**, *41* (4), 5967−5975.
(86) Predoi, D.; Iconaru, S. L.; Predoi, M. V.; Motelica-Heino, M.; Guegan, R.; Buton, N. Evaluation of Antibacterial Activity of Zinc-

Doped Hydroxyapatite Colloids and Dispersion Stability Using Ultrasounds. *Nanomaterials* **2019**, *9* (4), No. 515.
(87) Martinez-Zelaya, V. R.; Zarranz, L.; Herrera, E. Z.; Alves, A. T.; Uzeda, M. J.; Mavropoulos, E.; Rossi, A. L.; Mello, A.; Granjeiro, J. M.; Calasans-Maia, M. D.; Rossi, A. M. In Vitro and in Vivo Evaluations of Nanocrystalline Zn-Doped Carbonated Hydroxyapatite/Alginate Microspheres: Zinc and Calcium Bioavailability and Bone Regeneration. *Int. J. Nanomed.* **2019**, *14*, 3471−3490.
(88) Asghar, M. S.; Li, J.; Ahmed, I.; Ghazanfar, U.; Irshad, M. S.; Idrees, M.; Haq, Z.; Rizwan, M.; Sheikh, F.; Yasmeen, F. Antioxidant, and Enhanced Flexible Nano Porous Scaffolds for Bone Tissue Engineering Applications. *Nano Select* **2021**, *2* (7), 1356−1367.
(89) Guerra-López, J. R.; Bianchi, A. E.; Ramos, M. A.; Ubertino, M.; Ferraresi-Curotto, V.; Güida, J. A.; Barbaro, K.; Zhukova, A. A.; Grigorieva, V. Y.; Rau, J. V.; Echeverría, G. A. Preparation of Zinc-Doped Hydroxyapatite Ceramics and Evaluation of Biocompatibility and Antibacterial Activity. *J. Funct. Biomater.* **2025**, *16* (3), No. 88.
(90) Huang, W.; Xu, B.; Yang, W.; Zhang, K.; Chen, Y.; Yin, X.; Liu, Y.; Ni, Z.; Pei, F. Corrosion Behavior and Biocompatibility of Hydroxyapatite/Magnesium Phosphate/Zinc Phosphate Composite Coating Deposited on AZ31 Alloy. *Surf. Coat. Technol.* **2017**, *326*, 270−280.
(91) Akram, W.; Zahid, R.; Usama, R. M.; AlQahtani, S. A.; Dahshan, M.; Basit, M. A.; Yasir, M. Enhancement of Antibacterial Properties, Surface Morphology and In Vitro Bioactivity of Hydroxyapatite-Zinc Oxide Nanocomposite Coating by Electrophoretic Deposition Technique. *Bioengineering* **2023**, *10* (6), No. 693.
(92) Wang, B.; Li, Y.; Wang, S.; Jia, F.; Bian, A.; Wang, K.; Xie, L.; Yan, K.; Qiao, H.; Lin, H.; Lan, J.; Huang, Y. Electrodeposited Dopamine/Strontium-Doped Hydroxyapatite Composite Coating on Pure Zinc for Anti-Corrosion, Antimicrobial and Osteogenesis. *Mater. Sci. Eng., C* **2021**, *129*, No. 112387.
(93) Králová, Z. O.; Gorejová, R.; Oriňaková, R.; Petráková, M.; Oriňak, A.; Kupková, M.; Hrubovčáková, M.; Sopčák, T.; Baláž, M.; Maskalová, I.; Kovalčíková, A.; Kovaľ, K. Biodegradable Zinc-Iron Alloys: Complex Study of Corrosion Behavior, Mechanical Properties and Hemocompatibility. *Prog. Nat. Sci.: Mater. Int.* **2021**, *31* (2), 279−287.
(94) Yurchenko, E. V.; Ghileţchii, G. V.; Vatavu, S. A.; Petrenko, V. I.; Harea, D.; Bubulinca, C.; Dikusar, A. I. Composition, Structure, and Wear Resistance of Surface Nanostructures Obtained by Electric Spark Alloying of 65G Steel. *Surf. Eng. Appl. Electrochem.* **2024**, *60* (2), 194−203.
(95) Indra, A.; Gunawarman; Affi, J.; Mulyadi, I. H.; Wiyanto, Y. Physical and Mechanical Properties of Hydroxyapatite Ceramics with a Mixture of Micron and Nano-Sized Powders: Optimising the Sintering Temperatures. *Ceram.-Silik.* **2021**, *65* (3), 224−234.
(96) Han, K.; Lee, I.; Ohnuma, I.; Okuda, K.; Kainuma, R. Micro-Vickers Hardness of Intermetallic Compounds in the Zn-Rich Portion of Zn-Fe Binary System. *ISIJ Int.* **2018**, *58* (9), 1578−1583.

https://doi.org/10.1021/acsomega.5c08241
ACS Omega 2026, 11, 1062−1076